

Article

Reaction Mechanism for Methane-to-Methanol in Cu-SSZ-13: First-Principles Study of the $Z_2[\text{Cu}_2\text{O}]$ and $Z_2[\text{Cu}_2\text{OH}]$ Motifs

Unni Engedahl ^{1,2,*} , Adam A. Arvidsson ^{1,2} , Henrik Grönbeck ^{1,2}  and Anders Hellman ^{1,2,*} 

¹ Department of Physics, Chalmers University of Technology, 412 96 Göteborg, Sweden; adam.arvidsson@chalmers.se (A.A.A.); ghj@chalmers.se (H.G.)

² Competence Center for Catalysis, Chalmers University of Technology, 412 96 Göteborg, Sweden

* Correspondence: unni@chalmers.se (U.E.); ahell@chalmers.se (A.H.)

Abstract: As transportation continues to increase world-wide, there is a need for more efficient utilization of fossil fuel. One possibility is direct conversion of the solution gas bi-product CH_4 into an energy-rich, easily usable liquid fuel such as CH_3OH . However, new catalytic materials to facilitate the methane-to-methanol reaction are needed. Using density functional calculations, the partial oxidation of methane is investigated over the small-pore copper-exchanged zeolite SSZ-13. The reaction pathway is identified and the energy landscape elucidated over the proposed motifs $Z_2[\text{Cu}_2\text{O}]$ and $Z_2[\text{Cu}_2\text{OH}]$. It is shown that the $Z_2[\text{Cu}_2\text{O}]$ motif has an exergonic reaction path, provided water is added as a solvent for the desorption step. However, a micro-kinetic model shows that neither $Z_2[\text{Cu}_2\text{O}]$ nor $Z_2[\text{Cu}_2\text{OH}]$ has any notable activity under the reaction conditions. These findings highlight the importance of the detailed structure of the active site and that the most stable motif is not necessarily the most active.

Keywords: DFT; reaction mechanism; micro-kinetic model; small-pore zeolite; chabazite; SSZ-13; copper; methane-to-methanol; direct conversion



Citation: Engedahl, U.; Arvidsson, A.A.; Grönbeck, H.; Hellman, A. Reaction Mechanism for Methane-to-Methanol in Cu-SSZ-13: First-Principles Study of the $Z_2[\text{Cu}_2\text{O}]$ and $Z_2[\text{Cu}_2\text{OH}]$ Motifs. *Catalysts* **2021**, *11*, 17. <https://dx.doi.org/10.3390/catal11010017>

Received: 15 November 2020

Accepted: 15 December 2020

Published: 25 December 2020

Publisher's Note: MDPI stays neutral with regard to jurisdictional claims in published maps and institutional affiliations.



Copyright: © 2020 by the authors. Licensee MDPI, Basel, Switzerland. This article is an open access article distributed under the terms and conditions of the Creative Commons Attribution (CC BY) license (<https://creativecommons.org/licenses/by/4.0/>).

1. Introduction

The growing need for transportation makes a more efficient usage of combustion fuel necessary [1]. Methane, which is extracted together with crude oil, is a not fully utilized bi-product. As methane is a gas at standard conditions with high sunlight absorption properties, methane is often flared into CO_2 instead of being utilized [2]. Such a scenario can be avoided if it were possible to directly convert methane into methanol, which is a liquid at standard conditions. The management and distribution system is already in place to handle liquid fuels. The current method for methane-to-methanol (MTM) conversion is based on a large-scale two step process operating at high temperature and high pressure [3]. A major development would be a catalytic material that can transform methane into methanol in one step (direct methane-to-methanol (DMTM)) on a small scale, at low temperature and standard pressure.

The search for a catalyst for the partial oxidation of MTM has been the topic of many studies [4–7]. One line of research has been to mimic the porous structure and ionic metal sites of the naturally occurring enzymatic methane monooxygenases (MMOs) [8], which has been accomplished by metal ion-exchanged zeolites.

The basic building-blocks of zeolites are corner-sharing SiO_4 and AlO_4 tetrahedrons, with Si and Al tetrahedrally coordinated (T-site). A porous framework with pore sizes ranging from two to 12 membered rings (MRs) is formed by connecting tetrahedrons. One important characteristic of the zeolite system is the Si:Al ratio, which is commonly in the range of 5–20:1.

Experimentally, direct conversion of MTM over zeolites has been observed using a quasi-catalytic three step process: activation of the oxidant (O_2 , N_2O or NO) at high temperature (>350 °C); reaction phase at 50–210 °C and with the addition of CH_4 ; extraction

at 25–210 °C, where the reactants are flushed out using water/ethanol or some other solvent [9,10]. For instance, studies of the MFI zeolite ZSM-5 have shown catalytic activity for DMTM conversion, with the cation system of Cu-ZSM-5 being the most active for conversion [11]. However, the detailed configuration of the active site is still under debate [12–14]. An additional use of Cu-ZSM-5 is as a catalyst for the selective catalytic reduction reaction (SCR) of NO_x using NH₃ as the reducing agent [15]. However, the NH₃-SCR reaction is preferably performed over the small-pore chabazite system of Cu-SSZ-13 [16]. It is, thus, interesting to investigate whether Cu-SSZ-13 also would show activity for partial oxidation of methane [17–20].

Over the Cu₂O motif in Cu-ZSM-5, the reaction mechanism for direct conversion has been shown to occur via a three step reaction path: activation of the C–H bond in CH₄ over the active site and a rotation of the reactant, which leads to the formation of the CH₃OH-complex [11]. The active site in Cu-SSZ-13 has been suggested to be CuOH [21,22]. The proposed reaction mechanism [21] for CuOH is more complex than for Cu₂O in MFI. Direct insertion of a methyl radical can be done either with a possible two step reaction path or a five (alternatively six) step reaction path. The longer path shows an energy profile with low barriers. Furthermore, including water in the reaction path makes methanol formation energetically favourable [21]. However, the presence of the CuOH motif has also been explained as it is a possible precursor for the formation of either Cu₂O₂ or Cu₂O [23]. Larger Cu clusters (Cu > 2), namely Cu₃O₃ [24,25], have also been suggested as the active motif. The trimer structure has been shown to decrease the energy barrier for the activation of the C–H bond when compared with the smaller Cu monomer and dimer [21]. However, only large pore zeolites such as MFI and mordenite (MOR), are believed to contain these large clusters; in small pore zeolites, they have been shown to be unstable [22].

It has been shown that the active site motif is dynamic and depends sensitively on the operating conditions, such as the temperature and partial pressure of relevant gases [26,27]. Previous work [27] reports that for a quasi-catalytic reaction cycle in the zeolite Cu-SSZ-13 (with Si:Al = 10:2 and Al:Cu = 2:2, in the 12 T-site unit cell), the Cu₂OH motif, as seen in Figure 1a, is the energetically preferred structure for low temperature and low partial pressure of oxygen, while for high temperature and high partial pressure of oxygen, the Cu₂O motif, as can be seen in Figure 1b, is preferred. However, the reaction mechanism and character of the intermediates are not yet known.

In this study, we use first-principles calculations to determine the reaction mechanism for the partial methane oxidation over the active site motifs of Cu₂O and Cu₂OH in the small-pore zeolite SSZ-13. As water is often included as a solvent in the experimental procedure, its influence on the reaction mechanism is investigated in detail, and a micro-kinetic modelling is used to explore the activity of the considered sites.

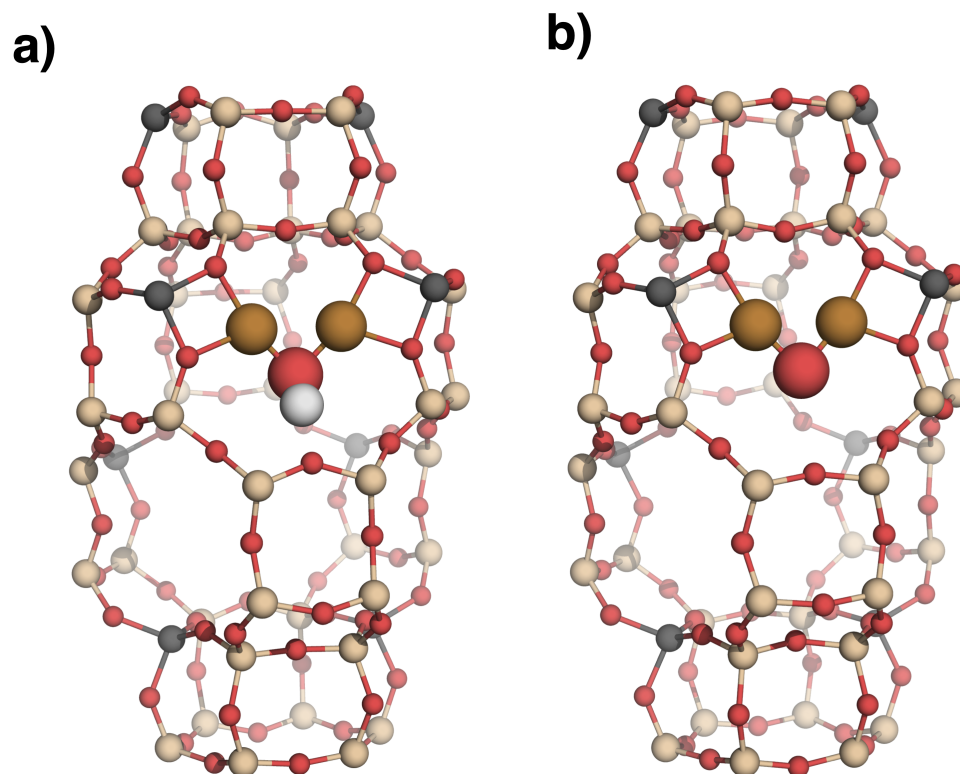


Figure 1. The two investigated active site structures and their positions in the zeolite framework are shown. In (a), the Cu_2OH site in SSZ-13 and in (b) the Cu_2O site in SSZ-13.

2. Results and Discussion

The reaction mechanism is elucidated for the reaction and the extraction phase of the DMTM reaction. This is experimentally done at 448 K and flow reactor conditions with 2% CH_4 and $10^{-9}\%$ CH_3OH with respect to atmospheric pressure [10]. Under these conditions, previous work has identified $\text{Z}_2[\text{Cu}_2\text{O}]$ and $\text{Z}_2[\text{Cu}_2\text{OH}]$, with the active sites situated in the 8MR in the chabazite (CHA) (see Figure 1a,b), as the most stable active site motifs [27].

In the description of the intermediate steps in the reaction mechanism, the two copper atoms of the active site are denoted as *. Hence, *X,Y implies that reaction intermediate X is coordinated to both Cu atoms, forming the current state of the active site, while reaction intermediate Y is either adsorbed on the active site or free in the zeolite.

The structural properties of gas phase H_2O , CH_4 and CH_3OH are in good agreement with the experimental values [28]; for details, see Table S1.

2.1. Reaction Mechanism over $\text{Z}_2[\text{Cu}_2\text{O}]$

The identified reaction mechanisms for DMTM at 448 K over $\text{Z}_2[\text{Cu}_2\text{O}]$ in SSZ-13 are presented in Figure 2, where the difference in the Gibbs free energy of two different mechanisms, with and without water, is compared (total energies for the mechanism can be found in Figure S2).

Starting with an empty zeolite, the free energy cost of moving one methane molecule into the zeolite framework is 0.28 eV. The first transition state (TS) is CH_4 dissociation, suggested to occur via a CH_3 radical [29]. Here, the methyl structure was found by constrained geometry optimizations and proved to be a saddle point through vibrational analysis and is shown as TS1 in Figure 2.

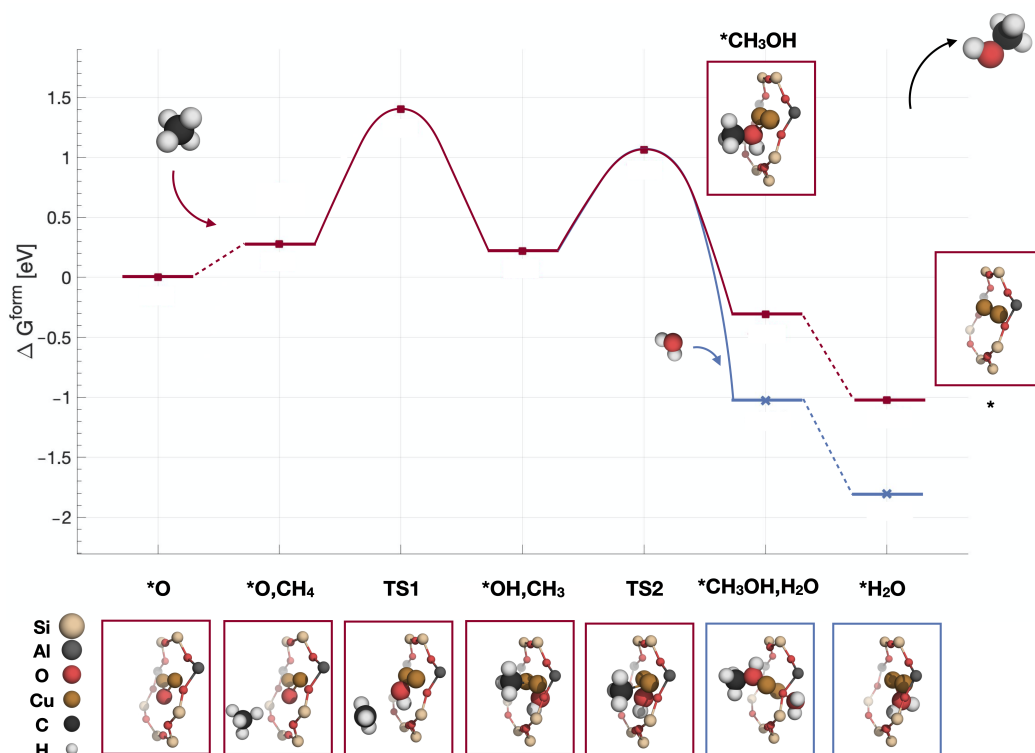


Figure 2. Reaction path over $Z_2[Cu_2O]$. Gibbs free energies are in eV and relative to that of $Z_2[Cu_2O]$ with CH_4 in the gas phase. The red squared path shows the reaction for dry conditions. Adding water to the mechanism gives the blue cross path. Both paths are exergonic. Reaction conditions are set to $T = 448$ K, $p_{CH_4} = 2\%$, $p_{H_2O} = 10\%$ and $p_{CH_3OH} = 10^{-9}\%$, with respect to atmospheric pressure. TS, transition state.

Passing through the methyl radical, with a barrier of 1.12 eV, the first intermediate step, i.e., $*OH, CH_3$ is an OH-group coordinated to both Cu atoms at a distance of 1.86/1.87 Å and a planar CH_3 at a distance of 2.08/2.07 Å. This configuration is 0.25 eV more stable than if CH_3 attaches to the framework. The second TS shows the carbon atom coordinating to one Cu atom at a distance of 2.15 Å and the OH-group lying in the plane of the 8MR. Under dry conditions ($p_{CH_4} = 2\%$, $p_{CH_3OH} = 10^{-9}\%$), the barrier to form an attached $*CH_3OH$ is 0.84 eV, where the oxygen in the methanol bridges both Cu atoms at a distance of 1.98/1.99 Å. The subsequent desorption energy of the CH_3OH molecule is 0.73 eV. The empty site after desorption is a $Z_2[Cu_2]$ structure with an interatomic distance of 2.46 Å, which is 0.07 Å larger than the Cu–Cu distance in the $Z_2[Cu_2O]$ structure. The energy is 1.84 eV higher than the most stable $Z_2[Cu_2]$ structure, where the copper atoms are situated in the 6MRs. This is clearly seen in the reactivity of the final structure. For instance, the adsorption energy of oxygen in the final structure, with the copper atoms residing in the 8MR as a reference, is -2.55 eV, as compared to -0.71 eV if using the most stable configuration as the reference.

The complete reaction under dry conditions, as marked by red squares in Figure 2, is exergonic by -1.02 eV. If water is added to the reaction mechanism after TS2, the methanol desorption becomes exergonic by -1.81 eV. This confirms the need for a solvent during the extraction phase [9,30]. The most exergonic reaction pathway ends in a $Z_2[Cu_2H_2O]$ structure with a Cu–Cu distance of 2.43 Å, Cu–O distances of 1.96/1.97 Å and a Cu–O–Cu angle of 76.3° . This is stretched and more acute as compared to the $Z_2[Cu_2O]$ structure of the original active site, where the distances are 2.39 Å and 1.74/1.74 Å and the angle 86° , respectively. In the energetic landscape, the relative energies of the reaction path show a decrease in energy when water is added (see Figure S2).

2.2. Reaction Mechanism over $Z_2[Cu_2OH]$

The Gibbs free energy along the reaction path under dry conditions, over the $Z_2[Cu_2OH]$ -site, is reduced to a one step reaction, marked by purple diamonds in Figure 3. The addition of water (blue crosses in Figure 3) to the mechanism adds one intermediate step and makes the reaction less exergonic. Total energies for the reaction path can be found in Figure S5.

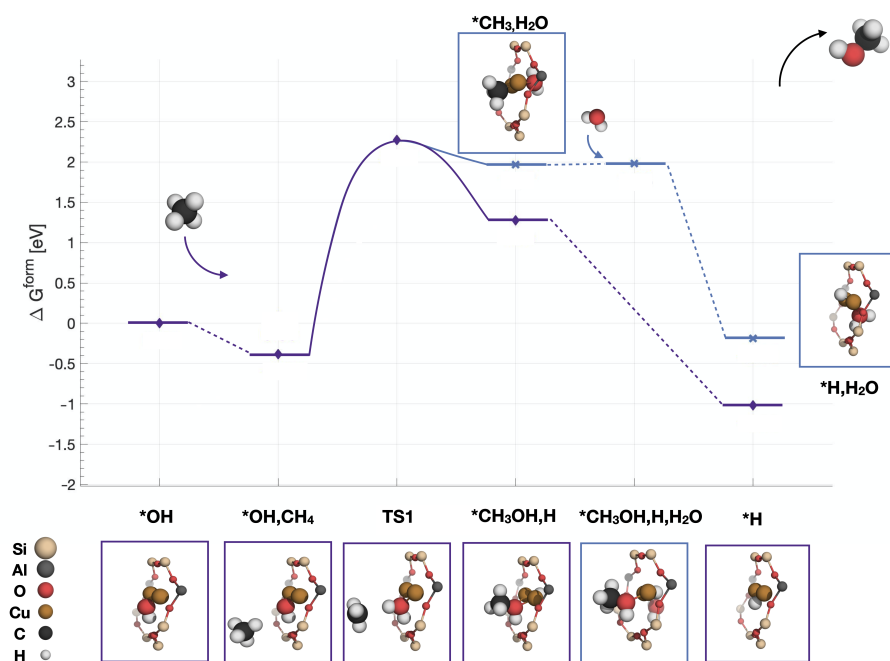


Figure 3. Reaction path over $Z_2[Cu_2OH]$. Purple diamonds mark the mechanism under dry conditions, blue cross the addition of one H_2O and grey triangles when two H_2O are included in the reaction. Gibbs free energies are in eV and relative to that of $Z_2[Cu_2OH]$ with CH_4 in the gas phase. Reaction conditions are set to $T = 448$ K, $p_{CH_4} = 2\%$, $p_{H_2O} = 10\%$ and $p_{CH_3OH} = 10^{-9}\%$, with respect to atmospheric pressure.

Starting with an empty zeolite, $*OH$, the introduction of methane into the zeolite is exergonic at -0.38 eV (treating the entropy of methane in the harmonic approximation increases the cost to 0.08 eV; see Figure S7). As in the $Z_2[Cu_2O]$ system, the methyl radical is found to have the lowest TS energy for CH_4 dissociation with a barrier of 2.65 eV.

Following the methyl radical along the dry path, the second intermediate ($*H,CH_3OH$) is 1.66 eV higher in energy than the first intermediate ($*OH,CH_4$). Methanol desorption is 2.30 eV lower in energy than the CH_3OH formation step in the reaction, and as a whole, the reaction is exergonic with 1.02 eV. The empty site after CH_3OH desorption is a Cu–H–Cu complex with a Cu–Cu distance of 2.34 Å, Cu–H bonds of $1.60/1.59$ Å and a Cu–H–Cu angle of 95° , displaying shorter bonds and a more obtuse angle when compared to the Cu–OH–Cu structure, where the distances are 2.50 Å and $1.82/1.82$ Å and the angle 86° .

All intermediates in the reaction are found to be doublets. The energy difference between the lowest and second lowest spin states is found in Table 1. A Bader analysis shows a charge of approximately $0.88/0.90$ on the Cu atoms for all but the final state, $*H$, where the charges instead are calculated to be $0.95/0.95$.

Table 1. Spin state of the intermediates in the reaction over $Z_2[Cu_2OH]$ following the reaction mechanisms in Figure 3. Energy difference between the two lowest spin states in eV.

Reaction Intermediate	Spin State	Energy Difference (eV)
*OH	doublet	3.60
*OH,CH ₄	doublet	3.60
TS1	doublet	1.84
*CH ₃ OH,H	doublet	3.42
*CH ₃ ,H ₂ O	doublet	3.05
*CH ₃ OH,H,H ₂ O	doublet	4.10
*H	doublet	3.55
*H,H ₂ O	doublet	3.51
*H,2(H ₂ O)	doublet	3.77

There is an additional path to the direct formation of CH₃OH on the $Z_2[Cu_2OH]$ structure. After the methyl TS1, an intermediate with a 0.18 eV lower formation energy than the direct formation of methanol, *CH₃OH,H, is found (see Figure S5). This is a CH₃-Cu₂-H₂O structure with a 0.69 eV higher free energy of formation (blue cross in Figure 3). To form methanol via this intermediate, water is included in the reaction, and the subsequent CH₃OH formation occurs at no cost. The CH₃OH molecule is attached to the Cu-H-Cu cluster on one side at a distance of 1.99 Å, and the H₂O molecule is on the other side at a distance of 2.08 Å. The most exergonic final state is that of $Z_2[Cu_2H]$ for completely dry conditions, i.e., including no water molecules. When water is included, the final state is a $Z_2[Cu_2H(H_2O)]$ structure with Cu-H bond of 1.59 and 1.58 Å and Cu-H₂O bonds of 2.17 and 2.14 Å, 0.83 eV higher in energy. The inclusion of water in the mechanism binds methanol stronger to the framework, hindering the desorption of the products. This is undesired and in contrast to established experimental procedure, where a solvent is introduced in order to extract the produced methanol [31]. Since the zeolite contains water [26,27], our results indicate that the participation of the $Z_2[Cu_2OH]$ site in the reaction is limited. In the energy landscape, the relative energies of the reaction path show a decrease in energy when water is added; see Figure S5.

2.3. Micro-Kinetic Model

With the help of a micro-kinetic model using the reaction paths shown in Figures 2 and 3, the performance of the active sites is analysed in Figure 4. The dry reactions over the $Z_2[Cu_2O]$ and $Z_2[Cu_2OH]$ sites in SSZ-13 are here compared to $Z_2[Cu_2O]H_2O$ in SSZ-13, as well as previous results for the same reaction over the $Z_2[Cu_2O]$ site in the large pore zeolite ZSM-5 [11]. In Figure 4a, the fraction of empty sites is plotted over time at a fixed temperature of 523 K, and Figure 4b shows the half-time of the sites as a function of temperature. The poor activity of the dry reactions over the sites in SSZ-13, as indicated in the free energies of the reaction landscape, is here confirmed. Additionally, due to the change in spin for TS1 in $Z_2[Cu_2O]$ SSZ-13 (as shown in Table 2), the rate is an upper limit.

The time needed to convert the active sites into CH₃OH is shown in Figure 4a. The MFI framework converted all active sites after 2 s. Second fastest is the Cu₂O site in CHA containing water (blue stars) at 9000 s; the Cu₂O site without water does not start the conversion until 316 years have passed, and the Cu₂OH site in CHA still has done no conversion at 10¹⁴ s. Treating the reactants according to the harmonic approximation instead of in the gas phase has no significant effect on the activity of the sites (see Figures S8 and S9).

The half-time of the sites as a function of temperature is shown in Figure 4b. The poorly performing systems show a clear increase in activity when the temperature is increased. Over the temperature range, the half-time for the $Z_2[Cu_2OH]$ SSZ-13 site is reduced from ~10¹⁶ s to ~10³ s. The $Z_2[Cu_2O]$ SSZ-13 is equally sensitive to a change in temperature, falling from ~10¹³ s to ~10² s. The two most active systems, $Z_2[Cu_2O]H_2O$ SSZ-13 and $Z_2[Cu_2O]$ ZSM-5, remain largely constant over the given temperature range. Here, it should be noted that the chabazite framework is only stable for temperatures below ~800 K [32].

Overall, the result shown in Figure 4 implies that neither the $Z_2[Cu_2O]$ nor $Z_2[Cu_2OH]$ site can be considered active sites for DMTM. However, the addition of H_2O to the $Z_2[Cu_2O]$ in SSZ-13 leads to a significant increase in the activity.

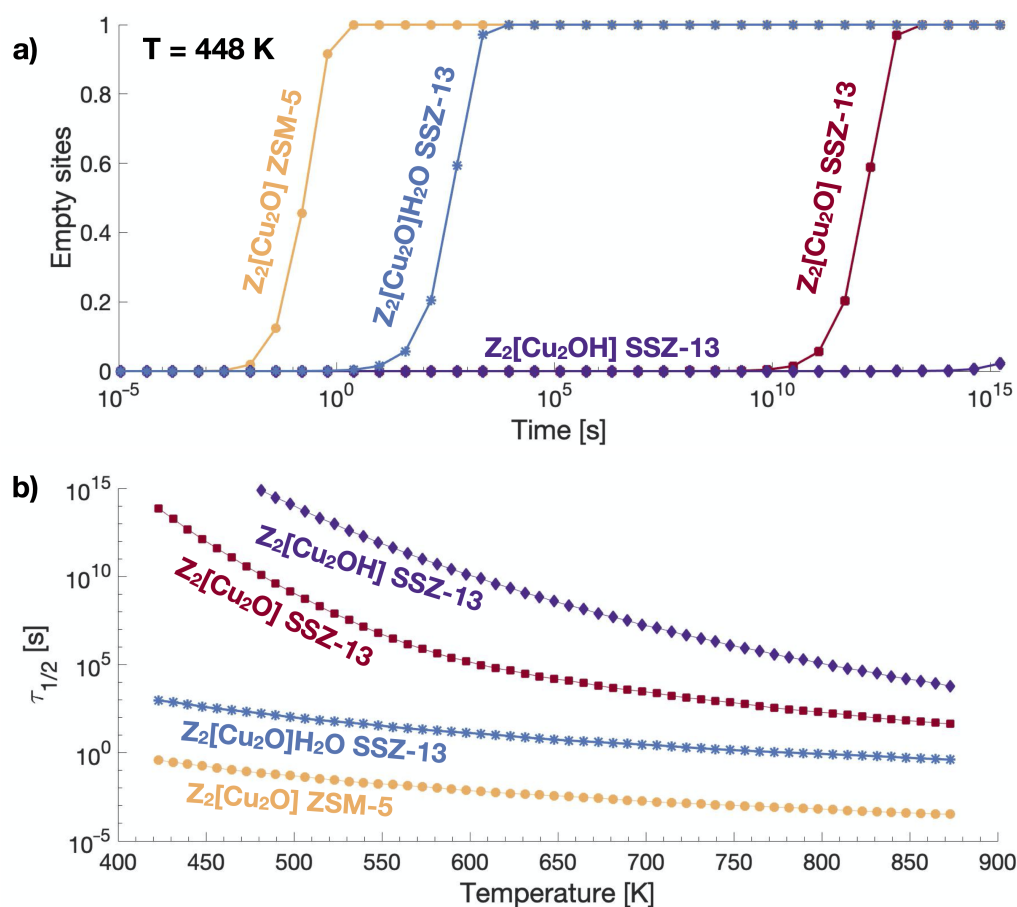


Figure 4. Coverages calculated for the reaction over four different sites: $Z_2[Cu_2O]$ in ZSM-5, $Z_2[Cu_2O]H_2O$ in SSZ-13, $Z_2[Cu_2O]$ in SSZ-13 and $Z_2[Cu_2OH]$ in SSZ-13. (a) shows transient kinetics and the fraction of empty sites as a function of time at a fixed temperature of 523 K. In (b), the half-time of the sites as a function of temperature is shown.

Table 2. Spin states of the intermediates in the reaction over $Z_2[Cu_2O]$ following the reaction mechanisms in Figure 2. The energy difference presented is that between the two lowest spin states in eV.

Reaction Intermediate	Spin State	Energy Difference (eV)
*O	singlet	0.03
*O,CH ₄	singlet	0.03
TS1	triplet	0.45
*OH,CH ₃	singlet	0.35
TS2	singlet	0.08
*CH ₃ OH	singlet	1.71
*CH ₃ OH,H ₂ O	singlet	2.01
*	singlet	0.26
*H ₂ O	singlet	1.69
*H ₂ O,H ₂ O	singlet	1.23

The reaction mechanism over $Z_2[Cu_2O]$ ZSM-5 is very similar to that over $Z_2[Cu_2O]$ SSZ-13, passing through a radical TS1 and then forming CH_3OH on the site [11]. However, as can be seen in Figure S10, it has a flatter energy landscape than that over $Z_2[Cu_2O]$ SSZ-

13; all barriers are lower in ZSM-5, as well as the final desorption step. Thus, comparing the activity of the two different zeolite frameworks, the $Z_2[\text{Cu}_2\text{O}]$ site in ZSM-5 is clearly more active than the sites in SSZ-13. In the transient kinetics in Figure 4, the $Z_2[\text{Cu}_2\text{O}]$ ZSM-5 sites are all consumed after ~ 0.6 s, and the site shows a half-time of 10^{-2} – 10^{-5} s. This higher activity corresponds well with experiments where large pore zeolites (such as ZSM-5 or mordenite) show higher turnovers for DMTM than small-pore zeolites (such as SSZ-13) [19].

3. Materials and Methods

Density functional calculations were performed using the Vienna Ab initio Simulation Package (VASP, Vienna, Austria) [33–38]. The projector augmented wave (PAW) method [39,40] is used to describe the interaction between the valence electrons and the core. PAW potentials were used with the valence states $\text{H}(1s^1)$, $\text{O}(2s^2 2p^4)$, $\text{C}(2s^2 2p^2)$, $\text{Al}(3s^2 3p^1)$, $\text{Si}(3s^2 3p^2)$ and $\text{Cu}(3d^{10} 4s^1)$. The exchange-correlation interaction was treated using the vdW-DF-cx functional [41–43], which includes van der Waals interactions in the exchange-correlation by taking non-local screening into account. In zeolites, the van der Waals interaction has been found to be important to include in the functional. Moreover, the Cu–O bond has shown sensitivity to the localization of the 3d-electrons [44]. The effect of using a +U correction of $U = 6$ eV is shown in Figures S3 and S6 for $Z_2[\text{Cu}_2\text{O}]$ and $Z_2[\text{Cu}_2\text{OH}]$, respectively. Overall, the adsorption energies of the reactants increases when the correction is applied.

The Kohn-Sham orbitals were represented using a plane wave basis set with 480 eV as the cut-off energy. A Gaussian smearing of 0.05 eV was applied to the Fermi-level discontinuity. The electronic energies were converged to 10^{-8} eV in the self-consistent loop, and ionic positions were considered to be relaxed when the largest atomic force in the system was smaller than 0.01 eV/Å. A Monkhorst-Pack grid with $2 \times 2 \times 2$ Γ -centred k-points was used to sample the Brillouin zone. The gas phase molecules were treated in a cubic box with sides of 10 Å. All calculations were done using spin polarization. All intermediate states were analysed for charge distribution using the Bader analysis method developed by the Henkelman group [45–48].

Vibrational energies were calculated by constructing the Hessian matrix using atomic forces generated by 0.01 Å displacements of the considered atoms. Only the extra-framework atoms, i.e., active site and reactants, were included in the vibration analysis. All low-lying normal wave numbers of the adsorbed reaction intermediate were set to 100 cm^{-1} (the included vibrations can be found in Tables S2 and S3). The translations and rotations of water, methane and methanol were calculated using the ideal gas approximation, whereas all vibrations were calculated using the harmonic approximation as implemented in the Thermochemistry module in the Atomic Simulation Environment (ASE) [49,50]. Rotations were treated by the rigid motor model [51]. The transition states (TSs) were characterized using the climbing nudged elastic band (NEB) method [52–54], during which the spin of the structure was allowed to change.

The stability of the reaction intermediate states was compared using the change in Gibbs free energy:

$$\Delta G(T, \Delta\mu) = \Delta H - T \cdot \Delta S(T) - \Delta\mu. \quad (1)$$

T is temperature, and $\Delta\mu$ is the change in chemical potential between 0 K and the condition of interest for the relevant gases. Here, $\Delta\mu = \Delta\mu_{\text{CH}_4}$, unless water is added into the mechanism, in which case, H_2O is treated in an analogous way to CH_4 in Equations (2) and (4) and $\Delta\mu$.

ΔS is the difference in entropy between the adsorbed and non-adsorbed state,

$$\Delta S = S(T, Z_2[\text{Cu}_2\text{OH}_{x+4}\text{C}]) - S(T, Z_2[\text{Cu}_2\text{OH}_x]), \quad (2)$$

where $Z_2[\text{Cu}_2\text{OH}_{x+4}\text{C}]$ and $Z_2[\text{Cu}_2\text{OH}_x]$ are the active sites inside the zeolite framework. When gas phase molecules are present in the zeolite cage, their entropy contribution is affected by the confinement of the zeolite structure and is calculated according to [55,56]:

$$S^{zeo} = \frac{2}{3} \left(S_{trans}^{gas} + S_{rot}^{gas} \right) + S_{vib}^{zeo}. \quad (3)$$

Here, S_{trans}^{gas} and S_{rot}^{gas} are the entropy contributions from the gas phase translations and rotations of the molecule, and S_{vib}^{zeo} is the entropy contribution from the vibrational modes of the molecule inside the zeolite. In Equation (1), the change in enthalpy is approximated as the difference in total energy [57] given by:

$$\Delta H \approx \Delta E = E_{Z_2[\text{Cu}_2\text{OH}_{x+4}\text{C}]} - E_{Z_2[\text{Cu}_2\text{OH}_x]} - E_{\text{CH}_4}. \quad (4)$$

3.1. Micro-Kinetic Modelling

The reaction pathways were explored using a mean-field micro-kinetic model for the DMTM reaction. The rate constants of the activated conversion of adsorbed reactants were expressed using the conventional transitions-state theory (TST) [51],

$$k_{\text{TST}} = \frac{k_B T}{h} \frac{Z^\ddagger}{Z} \exp\left(-\frac{\Delta E}{k_B T}\right), \quad (5)$$

where ΔE is the energy difference between the initial and transition state, Z is the partition function for the initial state, Z^\ddagger is the partition function for the transition state with the reaction coordinate excluded, k_B is Boltzmann's constant and h Planck's constant. The adsorption/desorption of methane and methanol was considered to be barrierless, and the rate constant for adsorption is calculated as:

$$k_{\text{ads}} = \frac{pA}{(2\pi mk_B T)^{1/2}}, \quad (6)$$

where p is the partial pressure of the molecule in the gas phase, A is the cross-sectional area of the pore and m the mass of the molecule. The corresponding desorption rate constants were obtained through the equilibrium constant:

$$K_{\text{eq}} = \frac{k_{\text{ads}}}{k_{\text{des}}} = \exp\left(-\frac{\Delta G}{k_B T}\right). \quad (7)$$

3.2. Zeolite Framework

In this study, the chabazite (CHA) framework SSZ-13 was used for catalysing the reaction. Considering the small 12 T-site unit cell of the CHA framework, an Si:Al ratio of 10:2 was used and denoted Z_2 . Comparisons were made with systems of a Si:Al ratio of 11:1, denoted Z . The cation introduced to compensate the 2+ charge in the Z_2 zeolite system was a Cu-dimer motif, which formed the active site. The reaction was performed over $Z_2[\text{Cu}_2\text{O}]$ and $Z_2[\text{Cu}_2\text{OH}]$; in a previous study identified to be the most stable motifs of the Cu-dimer under the reaction conditions [27].

4. Conclusions

The reaction mechanisms and the activity of DMTM conversion over $Z_2[\text{Cu}_2\text{O}]$ and $Z_2[\text{Cu}_2\text{OH}]$ in Cu-SSZ-13 are explored by first-principles calculations and micro-kinetic modelling. Over both systems, methane dissociation occurs via a methyl radical state, which is responsible for the highest barrier of the reaction in both systems. During dry reaction conditions: $T = 448 \text{ K}$, $p_{\text{CH}_4} = 2\%$ and $p_{\text{CH}_3\text{OH}} = 10^{-9}\%$ (with respect to atmospheric pressure); methanol desorption is exergonic over both structures. When water is added to the mechanism over $Z_2[\text{Cu}_2\text{O}]$, desorption becomes more exergonic; while in $Z_2[\text{Cu}_2\text{OH}]$, the addition of any water increases the cost of desorption.

The results show that neither of the dry sites ($Z_2[\text{Cu}_2\text{O}]$ and $Z_2[\text{Cu}_2\text{OH}]$) are responsible for any DMTM activity in SSZ-13 under the investigated conditions. Thus, for SSZ-13 to be considered as a candidate for the DMTM reaction, the conditions must be chosen with care; for instance by using a higher partial pressure of methane and including water. Another strategy would be to utilize other candidates for the active site that has a lower transition barrier for methane activation.

It should be noted that the identified reaction mechanism represents a quasi-catalytic cycle. The initial activation and subsequent reactivation of the active site are not taken into account. To close the cycle and make it a truly catalytic process remain as future challenges.

Supplementary Materials: The following are available online at <https://www.mdpi.com/2073-4344/11/1/17/s1>, Table S1: Molecular vibrations, Table S2: Vibrational frequencies of reaction intermediates in $Z_2[\text{Cu}_2\text{O}]$, Table S3: Vibrational frequencies of reaction intermediates in $Z_2[\text{Cu}_2\text{OH}]$, Figure S1: Unit cell and larger scale structure of SSZ-13, Figure S2: Reaction mechanism over $Z_2[\text{Cu}_2\text{O}]$ in relative energies, Figure S3: Reaction mechanism over $Z_2[\text{Cu}_2\text{O}]$ showing the effect of using +U, Figure S4: Reaction mechanism over $Z_2[\text{Cu}_2\text{O}]$ showing the change in free energy when using the harmonic approximation for reaction species, Figure S5: Reaction mechanism over $Z_2[\text{Cu}_2\text{OH}]$ in relative energies, Figure S6: Reaction mechanism over $Z_2[\text{Cu}_2\text{OH}]$ showing the effect of using +U, Figure S7: Reaction mechanism over $Z_2[\text{Cu}_2\text{OH}]$ showing the change in free energy when using the harmonic approximation for reaction species, Figure S8: Micro-kinetic model, Figure S9: Coverages, Figure S10: Reaction mechanism over Cu-ZSM-5 in relative energy.

Author Contributions: Conceptualization, H.G. and A.H.; methodology, U.E. and A.H.; software, U.E. and A.A.A.; validation, U.E., A.A.A. and A.H.; formal analysis, U.E. and A.A.A.; investigation, U.E. and A.A.A.; resources, H.G. and A.H.; data curation, U.E.; writing, original draft preparation, U.E.; writing, review and editing, U.E., A.A.A., H.G. and A.H.; visualization, U.E.; supervision, A.H.; project administration, H.G.; funding acquisition, H.G. All authors read and agreed to the published version of the manuscript.

Funding: Financial support is gratefully acknowledged from the Knut and Alice Wallenberg Foundation through the project “Atomistic design of catalysts” (No: KAW 2015.0058) and the Competence Centre for Catalysis (KCK) at Chalmers University of Technology. K.C.K. is financially supported by Chalmers University of Technology, the Swedish Energy Agency and the member companies: AB Volvo, ECAPS AB, Johnson Matthey AB, Preem AB, Scania CV AB and Umicore Denmark ApS. Calculations performed at C3SE at Chalmers, with CPU time provided through an SNIC grant.

Conflicts of Interest: The authors declare no conflict of interest.

References

1. U.S. Energy Information Administration (EIA). International Energy Outlook 2019. Available online: <https://www.eia.gov/outlooks/ieo/pdf/ieo2019.pdf> (accessed on 9 December 2020).
2. U.S. Energy Information Administration (EIA). Natural Gas Explained-Natural Gas and the Environment. Available online: <https://www.eia.gov/energyexplained/naturalgas/natural-gas-and-the-environment.php> (accessed on 9 December 2019).
3. Letcher, T. *Future Energy: Improved, Sustainable and Clean Options for our Planet*; Elsevier Science: Oxford, UK 2008.
4. Foster, N.R. Direct catalytic oxidation of methane to methanol—A review. *Appl. Catal.* **1985**, *19*, 1–11. [[CrossRef](#)]
5. Chun, J.W.; Anthony, R.G. Catalytic oxidations of methane to methanol. *Ind. Eng. Chem. Res.* **1993**, *32*, 259–263. [[CrossRef](#)]
6. Palkovits, R.; Antonietti, M.; Kuhn, P.; Thomas, A.; Schüth, F. Solid Catalysts for the Selective Low-Temperature Oxidation of Methane to Methanol. *Angew. Chem. Int. Ed.* **2009**, *48*, 6909–6912. [[CrossRef](#)] [[PubMed](#)]
7. Han, B.; Yang, Y.; Xu, Y.; Etim, U.; Qiao, K.; Xu, B.; Yan, Z. A review of the direct oxidation of methane to methanol. *Chin. J. Catal.* **2016**, *37*, 1206–1215. doi:10.1016/S1872-2067(15)61097-X. [[CrossRef](#)]
8. Sirajuddin, S.; Rosenzweig, A.C. Enzymatic Oxidation of Methane. *Biochemistry* **2015**, *54*, 2283–2294. [[CrossRef](#)]
9. Groothaert, M.H.; Smeets, P.J.; Sels, B.F.; Jacobs, P.A.; Schoonheydt, R.A. Selective Oxidation of Methane by the Bis(μ -oxo)dicopper Core Stabilized on ZSM-5 and Mordenite Zeolites. *J. Am. Chem. Soc.* **2005**, *127*, 1394–1395. [[CrossRef](#)]
10. Wang, X.; Martin, N.; Nilsson, J.; Carlson, S.; Gustafson, J.; Skoglundh, M.; Carlsson, P.A. Copper-Modified Zeolites and Silica for Conversion of Methane to Methanol. *Catalysts* **2018**, *8*, 545. [[CrossRef](#)]
11. Arvidsson, A.A.; Zhdanov, V.P.; Carlsson, P.A.; Grönbeck, H.; Hellman, A. Metal dimer sites in ZSM-5 zeolite for methane-to-methanol conversion from first-principles kinetic modelling: Is the $[\text{Cu}-\text{O}-\text{Cu}]^{2+}$ motif relevant for Ni, Co, Fe, Ag, and Au? *Catal. Sci. Technol.* **2017**, *7*, 1470–1477. [[CrossRef](#)]

12. Woertink, J.S.; Smeets, P.J.; Groothaert, M.H.; Vance, M.A.; Sels, B.F.; Schoonheydt, R.A.; Solomon, E.I. A $[\text{Cu}_2\text{O}]^{2+}$ core in Cu-ZSM-5, the active site in the oxidation of methane to methanol. *Proc. Natl. Acad. Sci. USA* **2009**, *106*, 18908–18913. [CrossRef]
13. Li, G.; Vassilev, P.; Sanchez-Sanchez, M.; Lercher, J.A.; Hensen, E.J.; Pidko, E.A. Stability and reactivity of copper oxo-clusters in ZSM-5 zeolite for selective methane oxidation to methanol. *J. Catal.* **2016**, *338*, 305–312. [CrossRef]
14. Hammond, C.; Forde, M.M.; AbRahim, M.H.; Thetford, A.; He, Q.; Jenkins, R.L.; Dimitratos, N.; Lopez-Sanchez, J.A.; Dummer, N.F.; Murphy, D.M.; et al. Direct Catalytic Conversion of Methane to Methanol in an Aqueous Medium by using Copper-Promoted Fe-ZSM-5. *Angew. Chem. Int. Ed.* **2012**, *51*, 5129–5133. [CrossRef] [PubMed]
15. Sjövall, H.; Blint, R.J.; Olsson, L. Detailed kinetic modelling of NH_3 SCR over Cu-ZSM-5. *Appl. Catal. Environ.* **2009**, *92*, 138–153. [CrossRef]
16. Kwak, J.H.; Tonkyn, R.G.; Kim, D.H.; Szanyi, J.; Peden, C.H. Excellent activity and selectivity of Cu-SSZ-13 in the selective catalytic reduction of NO_x with NH_3 . *J. Catal.* **2010**, *275*, 187–190. [CrossRef]
17. Oord, R.; Schmidt, J.E.; Weckhuysen, B.M. Methane-to-methanol conversion over zeolite Cu-SSZ-13, and its comparison with the selective catalytic reduction of NO_x with NH_3 . *Catal. Sci. Technol.* **2018**, *8*, 1028–1038. [CrossRef]
18. Newton, M.A.; Knorpp, A.J.; Pinar, A.B.; Sushkevich, V.L.; Palagin, D.; van Bokhoven, J.A. On the Mechanism Underlying the Direct Conversion of Methane to Methanol by Copper Hosted in Zeolites; Braiding Cu K-Edge XANES and Reactivity Studies. *J. Am. Chem. Soc.* **2018**, *140*, 10090–10093. [CrossRef] [PubMed]
19. Borfecchia, E.; Pappas, D.K.; Dyballa, M.; Lomachenko, K.A.; Negri, C.; Signorile, M.; Berlier, G. Evolution of active sites during selective oxidation of methane to methanol over Cu-CHA and Cu-MOR zeolites as monitored by operando XAS. *Catal. Today* **2019**, *333*, 17–27. [CrossRef]
20. Dinh, K.T.; Sullivan, M.M.; Narsimhan, K.; Serna, P.; Meyer, R.J.; Dincă, M.; Román-Leshkov, Y. Continuous Partial Oxidation of Methane to Methanol Catalyzed by Diffusion-Paired Copper Dimers in Copper-Exchanged Zeolites. *J. Am. Chem. Soc.* **2019**, *141*, 11641–11650. [CrossRef]
21. Kulkarni, A.R.; Zhao, Z.J.; Siahrostami, S.; Nørskov, J.K.; Studt, F. Monocopper Active Site for Partial Methane Oxidation in Cu-Exchanged 8MR Zeolites. *ACS Catal.* **2016**, *6*, 6531–6536. [CrossRef]
22. Yu Mao, P.H. Identification of the active sites and mechanism for partial methane oxidation to methanol over copper-exchanged CHA zeolites. *Sci. China Chem.* **2020**, *63*, 850–859. [CrossRef]
23. Ipek, B.; Wulfers, M.J.; Kim, H.; Göltl, F.; Hermans, I.; Smith, J.P.; Booksh, K.S.; Brown, C.M.; Lobo, R.F. Formation of $[\text{Cu}_2\text{O}]^{2+}$ and $[\text{Cu}_2\text{O}]^{2+}$ toward C–H Bond Activation in Cu-SSZ-13 and Cu-SSZ-39. *ACS Catal.* **2017**, *7*, 4291–4303. [CrossRef]
24. Wang, G.; Chen, W.; Huang, L.; Liu, Z.; Sun, X.; Zheng, A. Reactivity descriptors of diverse copper-oxo species on ZSM-5 zeolite towards methane activation. *Catal. Today* **2019**, *338*, 108–116. [CrossRef]
25. Mahyuddin, M.H.; Tanaka, T.; Shiota, Y.; Staykov, A.; Yoshizawa, K. Methane Partial Oxidation over $[\text{Cu}_2(\mu\text{-O})]^{2+}$ and $[\text{Cu}_3(\mu\text{-O})_3]^{2+}$ Active Species in Large-Pore Zeolites. *ACS Catal.* **2018**, *8*, 1500–1509. [CrossRef]
26. Paolucci, C.; Parekh, A.A.; Khurana, I.; Di Iorio, J.R.; Li, H.; Albarracin Caballero, J.D.; Shih, A.J.; Anggara, T.; Delgass, W.N.; Miller, J.T.; et al. Catalysis in a Cage: Condition-Dependent Speciation and Dynamics of Exchanged Cu Cations in SSZ-13 Zeolites. *J. Am. Chem. Soc.* **2016**, *138*, 6028–6048. [CrossRef] [PubMed]
27. Engedahl, U.; Grönbeck, H.; Hellman, A. First-Principles Study of Oxidation State and Coordination of Cu-Dimers in Cu-SSZ-13 during Methane-to-Methanol Reaction Conditions. *J. Phys. Chem. C* **2019**, *123*, 26145–26150. [CrossRef]
28. NIST Computational Chemistry Comparison and Benchmark Database, NIST Standard Reference Database Number 101. Available online: <https://cccbdb.nist.gov> (accessed on 21 October 2019)
29. Latimer, A.; Kulkarni, A.; Aljama, H.; Montoya, J.; Yoo, J.S.; Tsai, C.; Abild-Pedersen, F.; Studt, F.; Nørskov, J. Understanding trends in C–H bond activation in heterogeneous catalysis. *Nat. Mater.* **2016**, *16*. [CrossRef] [PubMed]
30. Sushkevich, V.L.; Palagin, D.; Ranocchiari, M.; van Bokhoven, J.A. Selective anaerobic oxidation of methane enables direct synthesis of methanol. *Am. Assoc. Adv. Sci.* **2017**, *356*, 523–527. [CrossRef]
31. Creci, S.; Wang, X.; Carlsson, P.A.; Martinelli, A.; Skoglundh, M. Methoxy ad-species in MFI zeotypes during methane exposure and methanol desorption followed by in situ IR spectroscopy. *Catal. Today* **2020**. doi:10.1016/j.cattod.2020.06.053. [CrossRef]
32. Schmieg, S.J.; Oh, S.H.; Kim, C.H.; Brown, D.B.; Lee, J.H.; Peden, C.H.; Kim, D.H. Thermal durability of Cu-CHA NH_3 -SCR catalysts for diesel NO_x reduction. *Catal. Today* **2012**, *184*, 252–261. doi:10.1016/j.cattod.2011.10.034. [CrossRef]
33. Kresse, G.; Hafner, J. Ab Initio molecular dynamics for liquid metals. *Phys. Rev. B* **1993**, *47*, 558–561. [CrossRef]
34. Kresse, G.; Furthmüller, J. Efficiency of Ab-Initio Total Energy Calculations for Metals and Semiconductors Using a Plane-Wave Basis Set. *Comput. Mater. Sci.* **1996**, *6*, 15–50. [CrossRef]
35. Kresse, G.; Furthmüller, J. Efficient Iterative Schemes for Ab Initio Total-Energy Calculations Using a Plane-Wave Basis Set. *Phys. Rev. B* **1996**, *54*, 11169–11186. [CrossRef] [PubMed]
36. Kresse, G.; Hafner, J. Norm-conserving and ultrasoft pseudopotentials for first-row and transition elements. *J. Phys. Condens. Matter* **1994**, *6*, 8245–8257. [CrossRef]
37. Klimes, J.; R Bowler, D.; Michaelides, A. Chemical accuracy for the Van der Waals density functional. *J. Phys. Condens. Matter* **2010**, *22*, 022201. [CrossRef] [PubMed]
38. Klimes, J.; Bowler, D.R.; Michaelides, A. Van der Waals density functionals applied to solids. *Phys. Rev. B* **2011**, *83*, 195131. [CrossRef]
39. Blöchl, P.E. Projector Augmented-Wave Method. *Phys. Rev. B* **1994**, *50*, 17953–17979. [CrossRef] [PubMed]

40. Kresse, G.; Joubert, D. From ultrasoft pseudopotentials to the projector augmented-wave method. *Phys. Rev. B* **1999**, *59*, 1758–1775. [[CrossRef](#)]
41. Dion, M.; Rydberg, H.; Schröder, E.; Langreth, D.C.; Lundqvist, B.I. Van der Waals Density Functional for General Geometries. *Phys. Rev. Lett.* **2004**, *92*, 246401. [[CrossRef](#)]
42. Lee, K.; Murray, E.D.; Kong, L.; Lundqvist, B.I.; Langreth, D.C. Higher-accuracy van der Waals density functional. *Phys. Rev. B* **2010**, *82*, 081101. [[CrossRef](#)]
43. Berland, K.; Hyldgaard, P. Exchange functional that tests the robustness of the plasmon description of the Van der Waals density functional. *Phys. Rev. B* **2014**, *89*, 035412. [[CrossRef](#)]
44. Chen, L.; Janssens, T.V.W.; Grönbeck, H. A comparative test of different density functionals for calculations of NH₃-SCR over Cu-Chabazite. *Phys. Chem. Chem. Phys.* **2019**, *21*, 10923–10930. [[CrossRef](#)]
45. Tang, W.; Sanville, E.; Henkelman, G. A grid-based Bader analysis algorithm without lattice bias. *J. Phys. Condens. Matter* **2009**, *21*, 084204. [[CrossRef](#)] [[PubMed](#)]
46. Sanville, E.; Kenny, S.; Smith, R. An Improved Grid-Based Algorithm for Bader Charge Allocation. *J. Comput. Chem.* **2007**, *28*, 899–908. [[CrossRef](#)] [[PubMed](#)]
47. Arnaldsson, A.; Jónsson, H. A Fast and Robust Algorithm for Bader Decomposition of Charge Density. *Comput. Mater. Sci. Comput. Mater. Sci.* **2006**, *36*, 354–360. [[CrossRef](#)]
48. Yu, M.; Trinkle, D. Accurate and efficient algorithm for Bader charge integration. *J. Chem. Phys.* **2011**, *134*, 064111. [[CrossRef](#)] [[PubMed](#)]
49. Larsen, A.H.; Mortensen, J.J.; Blomqvist, J.; Castelli, I.E.; Christensen, R.; Dułak, M.; Friis, J.; Groves, M.N.; Hammer, B.; Hargus, C.; et al. The atomic simulation environment—A Python library for working with atoms. *J. Phys.* **2017**, *29*, 273002.
50. Bahn, S.R.; Jacobsen, K.W. An object-oriented scripting interface to a legacy electronic structure code. *Comput. Sci. Eng.* **2002**, *4*, 56–66. [[CrossRef](#)]
51. Chorkendorff, I.; Niemantsverdriet, J.W. *Concepts of Modern Catalysis and Kinetics*; John Wiley & Sons: Weinheim, Germany 2006.
52. Sheppard, D.; Terrell, R.; Henkelman, G. Optimization methods for finding minimum energy paths. *J. Chem. Phys.* **2008**, *128*, 134106. [[CrossRef](#)]
53. Henkelman, G.; Jónsson, H. Improved tangent estimate in the nudged elastic band method for finding minimum energy paths and saddle points. *J. Chem. Phys.* **2000**, *113*, 9978–9985. [[CrossRef](#)]
54. Henkelman, G.; Uberuaga, B.P.; Jónsson, H. A climbing image nudged elastic band method for finding saddle points and minimum energy paths. *J. Chem. Phys.* **2000**, *113*, 9901–9904. [[CrossRef](#)]
55. Jørgensen, M.; Chen, L.; Grönbeck, H. Monte Carlo Potential Energy Sampling for Molecular Entropy in Zeolites. *J. Phys. Chem. C* **2018**, *122*, 20351–20357. [[CrossRef](#)]
56. Chen, L.; Janssens, T.V.W.; Vennestrøm, P.N.R.; Jansson, J.; Skoglundh, M.; Grönbeck, H. A Complete Multisite Reaction Mechanism for Low-Temperature NH₃-SCR over Cu-CHA. *ACS Catal.* **2020**, *10*, 5646–5656. [[CrossRef](#)]
57. Reuter, K.; Scheffler, M. Composition, structure, and stability of RuO₂(110) as a function of oxygen pressure. *Phys. Rev. B* **2001**, *65*, 1–11. [[CrossRef](#)]